Design and Optimization of Infrared Radiation Barrier Using Omnidirectional Reflectors

Shihe Pan,[a,b,#] Yixin Sun,[a,#] Xiaoquan Liu,[a] Xiaoqi Zhou,[a] Shipei Zhang,[a] Shengyu Sun,[a] and Xiawa Wang[a,*]

AUTHOR ADDRESS

[a]Division of Natural and Applied Sciences, Duke Kunshan University, Suzhou 215316, China

[b]Current address: Electrical and Computer Engineering Department, University of California, Los Angeles, CA 90095, USA

AUTHOR INFORMATION

*Corresponding Author

E-mail address: xiawa.wang@dukekunshan.edu.cn (X. Wang)

[#]S. Pan and Y. Sun contributed equally to this work

ABSTRACT: In this work, we designed and optimized a one-dimensional (1D) photonic crystal (PhC) for the application of a thermal radiation barrier. The insulation relies on the omnidirectional bandgap to reflect electromagnetic radiation regardless of its incident angle and polarization. As thermal radiation has a broadband spectrum that depends on both wavelength and angle, a cascaded and differentiated waveband design was utilized. The optimized omnidirectional reflector (ODR) is composed of germanium (Ge) and magnesium fluoride (MgF_2), consisting of 4 differentiated patterns with 2 periods each to have the maximum insulation performance within reasonable fabrication costs. For a 1200 K blackbody radiator, the heat retaining rate can reach 93.5% within a thickness of 13 μm. We analyzed the role of each pattern and substantiated the methodology of differentiated waveband design, which can be generalized to other photonic designs for thermal insulation. We further assessed potential uncertainties induced by fabrication processes and material properties. The reflector can retain above 90% of the radiative heat from high-temperature sources when the thickness variation is within 13% of the designed values, even incorporating the largest optical constant differences used in this work. The broadband ODR with a differentiated design may provide an optimal solution to insulate radiative heat for ultra-high temperature and small-scale heat sources, surpassing conventional solutions provided by metallic coating or multilayer insulation.

KEYWORDS thermal insulator, omnidirectional reflector, photonic crystal, radiative insulation barrier

INTRODUCTION

Driven by the rapid advancement of the modern economy, there is an increasing demand for compact and efficient energy sources. Thermal-based power generators have gained increasing attention because heat generation is usually simple and cost-effective. According to the second law of thermodynamics, the efficiency of a heat engine is related to the temperature difference between source and sink — the larger the difference, the higher the theoretical conversion efficiency. Many cutting-edge technologies, such as high-temperature fuel cells [1], ultra-micro scale gas turbines [2], micro-sized Stirling engines [3], and radioisotope power generators [4–6], as illustrated in **Fig. S1**, all rely on high temperatures to drive reactions for electricity generation. Among these small-scale high-temperature power generators, thermophotovoltaic (TPV) systems have emerged as particularly promising due to several advantages, including high efficiency, silent operation, direct DC power generation, and ease of miniaturization [5]. In particular, small-scale TPV systems are well-suited for portable power sources based on combustion chamber and radioisotope generators, providing a reliable and long-duration energy supply for mini-satellites and spacecraft in deep-space missions [5,6].

TPV systems typically operate at high temperatures exceeding 900 °C, consistent with the requirements of available low-bandgap photovoltaic (PV) cells [7]. However, this presents significant challenges for thermal insulation in small-scale systems, as their outer surfaces must remain near room temperature to prevent thermal hazards. The large temperature gradient over a short distance necessitates the design of an efficient thermal radiation barrier, requiring careful engineering to retain heat while ensuring that the cold side remains safe to touch [8,9]. While thermal insulation in TPV systems remains underexplored, various reflection-based thermal radiation barriers have been studied in aerospace and nuclear fields. Metallic coatings, such as gold and titanium, have been employed for thermal shielding but suffer from instability at extreme temperatures due to degradation and diffusion [10,11]. Non-contact enclosures with reflective metal foils offer an alternative; however, most refractory metals reflect less than 80% of infrared radiation, except for gold, which is too costly and malleable [12]. Moreover, the high absorption of metals leads to heat buildup, causing them to function as secondary emitters. Thermal barrier coatings (TBCs), including ceramic-based photonic crystals (PhCs) and

photonic glasses (PhGs), have shown promise for high-temperature insulation [13–18]. However, most TBCs are designed for gas turbines, where conduction and convection dominate heat transfer, necessitating the use of high-temperature ceramic materials such as yttrium-stabilized zirconia (YSZ) and alumina (Al_2O_3). Even with carefully engineered 1D–3D photonic structures, their average reflectance remains around 70–80%, which is insufficient for effective TPV insulation. Multilayer insulators (MLIs), originally developed for space applications [19], provide reliable high-temperature thermal insulation using metallic reflectors separated by low-conductivity spacers [20], achieving thermal conductivities as low as 0.01–0.05 W/m·K. [21–23]. However, their bulky design, which requires millimeter-scale spacing between layers, poses integration challenges in compact TPV system [24]. These limitations underscore the need for new materials capable of efficient thermal radiation management in TPV systems.

In this study, we propose the use of a dielectric omnidirectional reflector (ODR) as a thermal radiation barrier, specifically targeting small-scale high-temperature TPV systems. Our design offers a broad reflection bandwidth, high reflectance, minimal thickness, and relatively simple fabrication. Omnidirectional reflection, first introduced by Winn et al. [25] and realized by Fink et al. [26], is widely used in photonics for dielectric mirrors and radiation control [27,28]. While most existing ODR designs feature narrow bandgaps as summarized in supplementary **Table S1** [26,29–36], which limits their application in thermal radiation shielding, our novel ODR design integrates cascaded 1D PhCs to achieve broader reflection and optical insulation. The proposed design is adaptable to different heat sources, with adjustable bandgap sizes and differentiated functions for enhanced performance. We present optimal designs for various heat source temperatures and evaluate their performance and fabrication feasibility, with total ODR thicknesses ranging from 10–20 μm, thereby overcoming the size limitations of MLIs.

THEORY AND METHODS

High-temperature heat sources typically exhibit a broadband spectrum ranging from near-infrared to mid-infrared. To effectively block broadband radiation using ODRs, multiple photonic bandgaps need to be overlapped, as illustrated in **Fig. 1**a. This approach shields the

entire spectrum through a cascaded design, a technique commonly employed in past research to enlarge the overall bandgap size [37–41]. In such a design, the photonic bandgap of each ODR pattern can be tailored by ensuring a sufficiently large refractive index contrast between the two materials, as well as an appropriate ratio (>1) between the low refractive index and the ambient refractive constant.[42] **Fig. 1**b shows the theoretical bandgap size of a 1D PhC as a function of its central wavelength for various optical contrasts. Under ideal conditions (i.e., a semi-infinite structure and normal incidence), an approximate analytical expression for the extent of omnidirectional gaps can be derived from Equation 1 and 2.

$$\omega_h = \frac{2c}{t_2 n_2 + t_1 n_1} \cos^{-1}\left(-\left|\frac{n_1 - n_2}{n_1 + n_2}\right|\right) \tag{1}$$

$$\omega_l = \frac{2c}{t_2\sqrt{n_2^2 - n_0^2} + t_1\sqrt{n_1^2 - n_0^2}} \times \cos^{-1}\left(\left|\frac{n_1^2\sqrt{n_2^2 - n_0^2} - n_2^2\sqrt{n_1^2 - n_0^2}}{n_1^2\sqrt{n_2^2 - n_0^2} + n_2^2\sqrt{n_1^2 - n_0^2}}\right|\right) \tag{2}$$

where ω_h and ω_l are the upper and lower angular frequency boundaries of the bandgap, n_1 and n_2 are the high and low refractive indices, n_0 is the ambient refractive constant, t_1 and t_2 are the quarter-wavelength thicknesses for each dielectric material, and c is the speed of light [26]. In this work, we chose germanium (Ge, $n \approx 4.25$) and magnesium fluoride (MgF_2, $n \approx 1.36$) as the high and low refractive index materials, respectively. These two dielectric materials provide one of the highest possible contrasts extending to mid-infrared and have been proven compatible with fabrication processes [43]. Within the wavelengths of interest, both materials exhibit high stability of refractive indices with nearly zero extinction coefficients, resulting in minimal absorption losses.

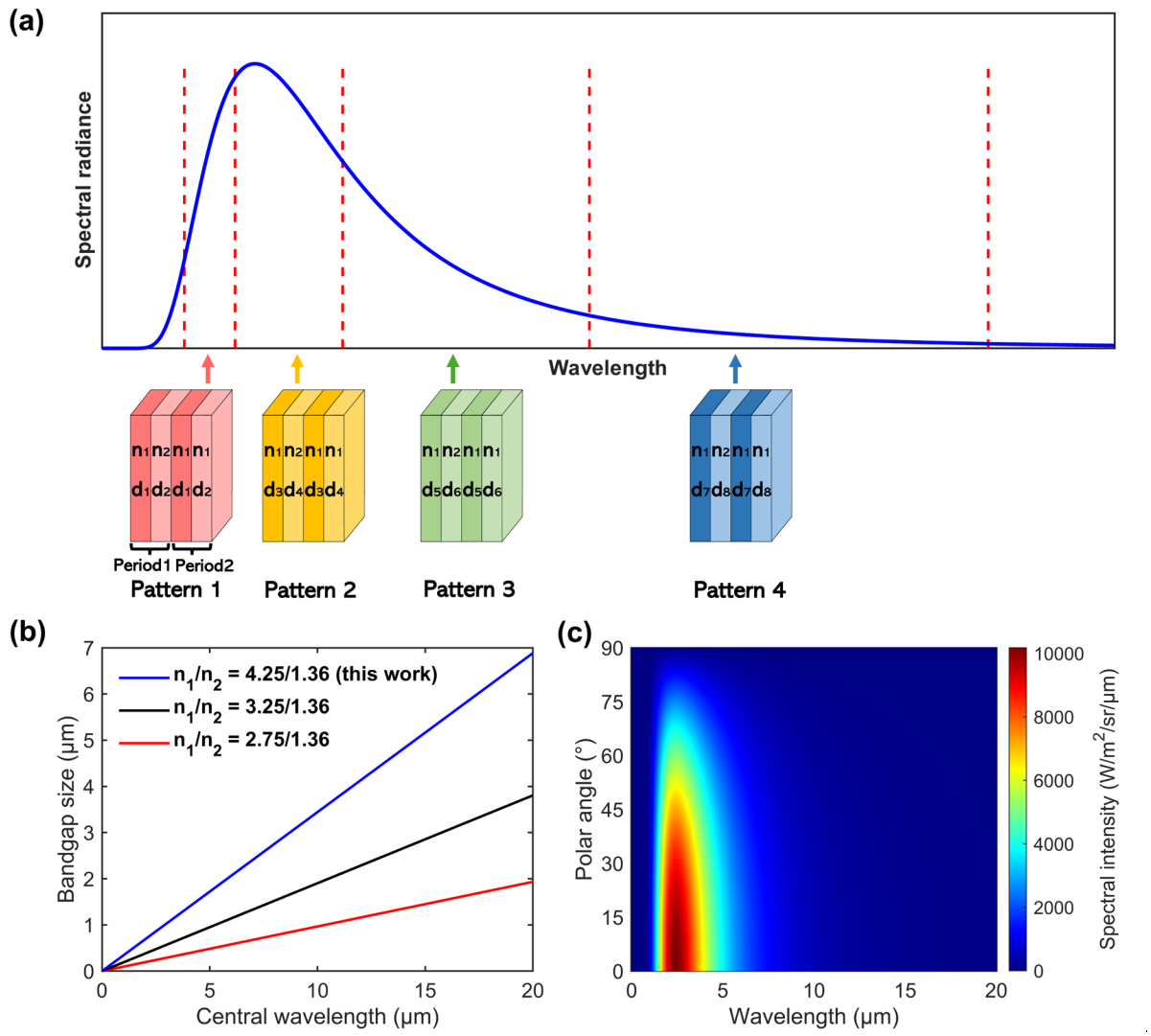

Fig. 1. Conceptual design of an ODR as a thermal radiation barrier. (a) A general blackbody radiation spectrum is divided into four segments, each insulated by a 1D PhC composed of 2 periods. (b) Photonic bandgap size of ODRs as a function of central wavelength, shown for different optical contrasts under ideal conditions (assuming quarter-wavelength thicknesses). (c) Wavelength and polar angle dependence of radiation emitted from a 1200 K blackbody radiator.

In the radiative heat transfer model, a blackbody surface has maximum emissivity and emits non-polarized electromagnetic waves with a polar-angle dependence but no azimuthal-angle dependence. In practice, real surfaces may deviate from this ideal model by having directional and spectral dependence on emissivity. However, the ideal blackbody heat source represents the most challenging shielding scenario without losing the generality of real surfaces and was

therefore adopted in our design. **Fig. 1**c presents the radiation spectrum of an ideal blackbody surface at 1200 K, where the wavelength dependence follows Planck's law and the angle dependence adheres to Lambert's cosine law. To effectively shield thermal radiation, angle dependence must be considered with equal or greater priority than wavelength dependence for two reasons, as detailed in **Fig. S2**. First, both theoretical predictions and experimental results indicate that the near-perfect reflection range of ODRs narrows and becomes less effective as the incident angle increases. Second, blackbody intensity remains high near the peak wavelength at large angles, whereas it is significantly lower far from the peak, even at normal incidence. To compensate for radiation loss due to increased incident angles and material absorption, we designed a cascaded ODR composed of four patterns with distinct functions, i.e., differentiated waveband design. Since Ge exhibits a high extinction coefficient at short wavelengths, the 1st pattern is optimized to suppress material absorption while reflecting short-wavelength radiation. The middle two patterns function as conventional reflectors, maximizing shielding in the spectral region where thermal radiation is strongest. The last pattern is specifically designed as a compensation structure to further suppress the emission at large angles in the mid-wavelength range. In other words, the 4th pattern enhances the performance of the 2nd and 3rd patterns by addressing their strong angular selectivity. All the patterns were brought together into the simulation incorporated with ideal blackbody spectra and real optical constants to achieve the highest overall reflectance.

In a TPV system, as shown in **Fig. 2**a, the ODR is used to encapsulate surfaces of the heat source that do not contribute to energy conversion. These non-emitting surfaces typically require effective insulation to raise the source temperature—an important consideration in many TPV systems, especially with a fixed amount of heat input like radioisotopes or combustions. In contrast, the source surface equipped with the selective emitter remains exposed and is oriented toward the TPV cell at a mesoscale distance. As illustrated in **Fig. 2**b, the ODR is positioned close to the heat source without physical contact, secured either by localized adhesive bonding or an external support structure. A vacuum gap between the ODR and the heat source minimizes conductive heat transfer, enabling the ODR to act primarily as a radiative barrier (**Fig. 2**d). By reflecting thermal radiation back toward the source, the ODR

improves thermal confinement while maintaining a lower operating temperature, thereby reducing the risk of degradation or delamination. To evaluate its effectiveness as a thermal radiation barrier, it is essential to consider the framework of radiative heat transfer. Our analysis is based on three key assumptions: (1) The ODR is an optically smooth dielectric mirror with only specular reflection. (2) The ODR has no local emission because it is maintained at a much lower temperature than the heat source. It has minimal absorption due to the small extinction coefficients of dielectric materials. (3) The ODR encloses the heat source, with radiative heat transfer as the only mode of heat exchange between the two. The heat source is approximated as a diffuse blackbody emitter following Lambert's cosine law, while the ODR is modeled as a non-emissive surface with wavelength-dependent reflectivity. Thermal emission in the direction $\hat{\mathbf{s}}'$ originates from a differential element on the heat source and is reflected by the ODR into the direction $\hat{\mathbf{s}}$. Based on this setup, the radiation loss (%), as the primary figure of merit (FOM) for optimization, is expressed by the following equations.

$$Radiation\ Loss\ (\%) = \frac{J_{source} - H_{source}}{J_{source}} = 1 - \frac{H_{source}}{J_{source}} \tag{3}$$

$$= 1 - \frac{\int_0^\infty \int_\Omega I_{b\lambda}(\boldsymbol{r}', \hat{\boldsymbol{s}}', \lambda)\rho_\lambda(\boldsymbol{r}, \hat{\boldsymbol{s}}, \lambda)\cos\theta_i d\Omega_i d\lambda}{\sigma T^4} \tag{4}$$

$$= 1 - \frac{\int_0^\infty \int_0^{2\pi} \int_0^{\frac{\pi}{2}} I_{b\lambda}(\lambda)\, \rho_\lambda(\theta_i, \lambda)\cos\theta_i \sin\theta_i d\theta_i d\varphi d\lambda}{\sigma T^4} \tag{5}$$

Following the convention in radiative heat transfer studies [44], J_{source} is the radiosity, H_{source} is the irradiance, $I_{b\lambda}(\boldsymbol{r}', \hat{\boldsymbol{s}}', \lambda)$ is the spectral blackbody intensity, $\rho_\lambda(\boldsymbol{r}, \hat{\boldsymbol{s}}, \lambda)$ is the spectral bidirectional reflection function of reflectors, θ_i is the incident angle, and Ω_i is the incident solid angle. Here, $\boldsymbol{r}$ and $\hat{\boldsymbol{s}}$ are the position and unit direction vectors ($\boldsymbol{r}', \hat{\boldsymbol{s}}'$ for heat source; $\boldsymbol{r}, \hat{\boldsymbol{s}}$ for reflector). Radiation loss is expressed as the ratio of net radiation flux q ($q = J_{source} - H_{source}$) to radiosity of the heat source. As the heat source is assumed to be an ideal blackbody, its radiosity J_{source} is simply given by the total emissive power σT^4, where σ is the Stefan-Boltzmann constant. In this setup, the radiation reflected back by the ODR is the only source of irradiance. Thus, the heat source's irradiance H_{source} is expressed as the integral of the product of spectral blackbody intensity and spectral reflection function, both of which are wavelength-dependent. The equation can be further simplified into a calculable form,

considering that spectral blackbody intensity depends solely on temperature and wavelength, while reflectivity depends only on incident angle and wavelength.

The optimization was performed using the Stanford Stratified Structure Solver (S^4) based on Rigorous Coupled Wave Analysis (RCWA) in an iterative approach [45]. Starting with a theoretically computed structure as the initial design, a systematic coordinate-wise search was conducted, where each layer's thickness was independently varied, and the corresponding radiation loss was calculated to identify local minima across different designs. The most promising solutions were then iteratively refined, adjusting the thicknesses collectively within tighter parameter ranges until the lowest FOM was reached. Real optical constants of Ge and MgF_2 concatenated from various sources were used in optimization, as shown in **Fig. 2**c [46,47]. Additionally, the optical constants at different temperatures were substituted into the optimized structure to evaluate the impact of temperature variations on performance. To obtain the temperature-dependent refractive indices of MgF_2, its structural and electronic properties were calculated using density functional theory (DFT) in the Quantum ESPRESSO package [48], and optical properties were subsequently carried out using the Yambo package [49]. A scalar relativistic norm-conserving pseudopotential description, generated with a Perdew-Burke-Ernzerhof (PBE) exchange-correlation functional, was used. A kinetic energy cutoff of 45 Ry was applied for the plane-wave basis of MgF_2. A uniform 3×3×5 k-points mesh was employed in the lattice for the integration over the Brillouin zone. The lattice parameters were a = 4.62 Å, and c = 3.05 Å for MgF_2. Quasiparticle (QP) correction on the electronic band structure was introduced using the non-self-consistent Green's function/Screen Coulomb interaction (GW) approach as implemented in Yambo software. A total of 40 bands (16 unoccupied) were considered in the static screening for MgF_2. In the excited state calculations, a 0.01 eV damping coefficient was used as the width of the Lorentzian peaks of optical spectra under finite temperatures. The real and imaginary components of the electric permittivity were obtained at 300 K, 500 K, and 700 K for MgF_2.

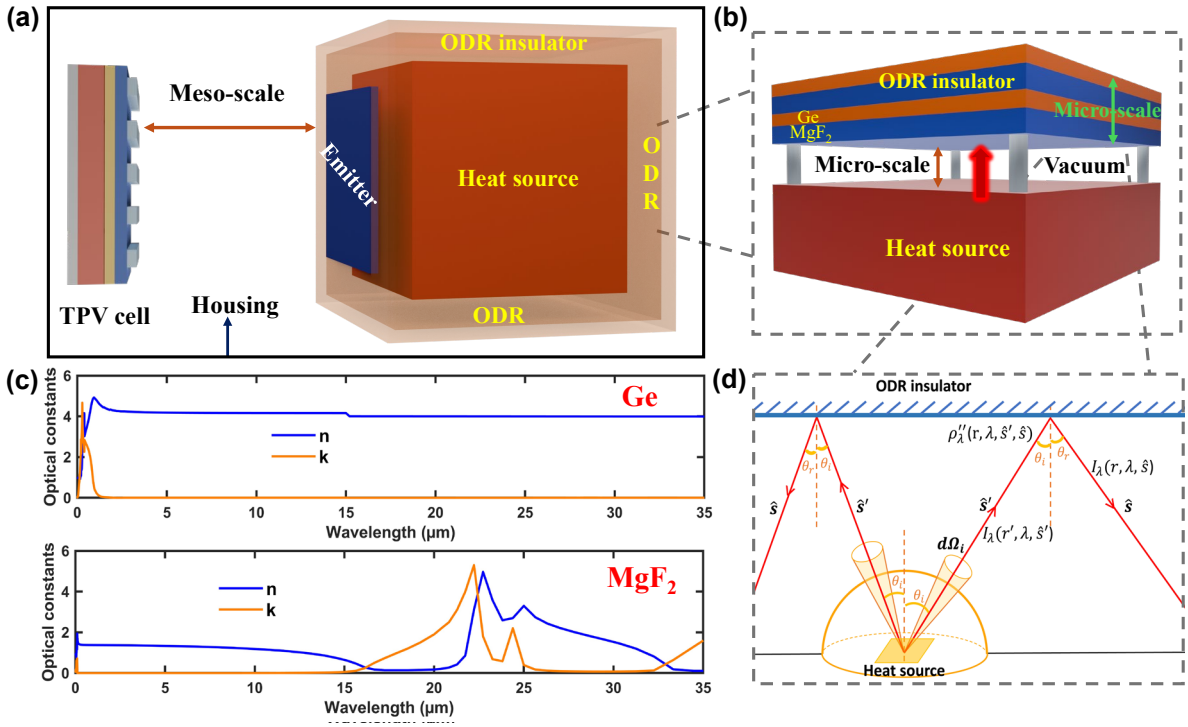

Fig. 2. Geometrical representation and material selection for an ODR as a thermal radiation barrier. (a) Schematic illustration of the application scenario of the ODR insulator within a complete TPV system. (b) Schematic illustration depicting the integration between the heat source and the insulator. (c) Optical constants of Ge and MgF_2 used in this study. Data were compiled from various sources [46,47]. (d) Geometrical illustration of the radiative interaction between the heat source and the insulator.

RESULTS AND DISCUSSION

We optimized ODRs consisting of 4 patterns with 2 periods each (16 layers in total), for blackbody heat sources ranging from 800 K to 1400 K. The detailed structures are provided in **Table 1**. At normal incidence, each pattern in the reflector is designed to shield radiation within a specific wavelength range. Taking the optimized design at 1200 K as an example, **Fig. 3**a presents the reflectance spectrum from 0 to 20 μm, while the corresponding band structure in **Fig. S3** confirms the presence of omnidirectional bandgaps. Although the ODR was simulated and optimized as a whole, we introduced each pattern separately into the simulation as an independent reflector to better visualize its bandgap coverage and illustrate the cascaded design. The resulting spectra, shown in different colors, highlight each pattern's contribution. In the spectral range near the blackbody's peak wavelength (primarily shielded by the 2nd and 3rd

patterns), the structure exhibits high reflectance to block the majority of the energy. The shielding effect diminishes for spectral ranges below 1 μm and above 16 μm. To shield high-energy photons in the visible regime, the photonic design must shrink the characteristic dimension below 100 nm with layer precision in nanometers, inducing significant fabrication challenges. The leakage above 16 μm mainly arises from the decreasing refractive index of MgF_2, as shown in **Fig. 2**c. Combining these results with the spectral intensity of a 1200 K blackbody, the radiation loss through the insulator at normal direction is depicted in **Fig. 3**b. The ODR with a total thickness of 12.64 μm is able to effectively shield most of the energy, allowing only 6.51% of the radiation to be absorbed or transmitted. For other temperatures, the overall radiation loss ranges from 6.51% to 8.44%. The performance of reflectors degrades slightly at lower temperatures compared to the higher ones, possibly due to the increased impact of the non-ideal optical constants of MgF_2 at long wavelengths. Notably, the optimal material thickness has an inverse relation to the source temperature. As the source temperature decreases, the emission spectrum extends to longer wavelengths, resulting in thicker structures and more costly fabrication. Therefore, ODRs are most effective for shielding heat sources above 1000 K, which aligns with the operating temperatures of most TPV systems.

Table 1. The optimized structures of ODRs for various heat source temperatures.

Source temperature (K)	Pattern 1		Pattern 2		Pattern 3		Pattern 4		Radiation loss
	t_{MgF2} (nm)	t_{Ge} (nm)	t_{MgF2} (nm)	t_{Ge} (nm)	t_{MgF2} (nm)	t_{Ge} (nm)	t_{MgF2} (nm)	t_{Ge} (nm)	
800	804.4	150.8	1407.8	280.1	2145.2	646.4	3687.0	1228.2	8.44%
1000	533.1	102.8	959.6	205.7	1439.3	445.6	2612.1	857.0	6.91%
1200	487.3	85.1	841.7	184.3	1284.7	382.8	2303.7	751.4	6.51%
1400	453.3	72.5	793.2	157.2	1171.0	350.6	2115.3	677.1	6.84%

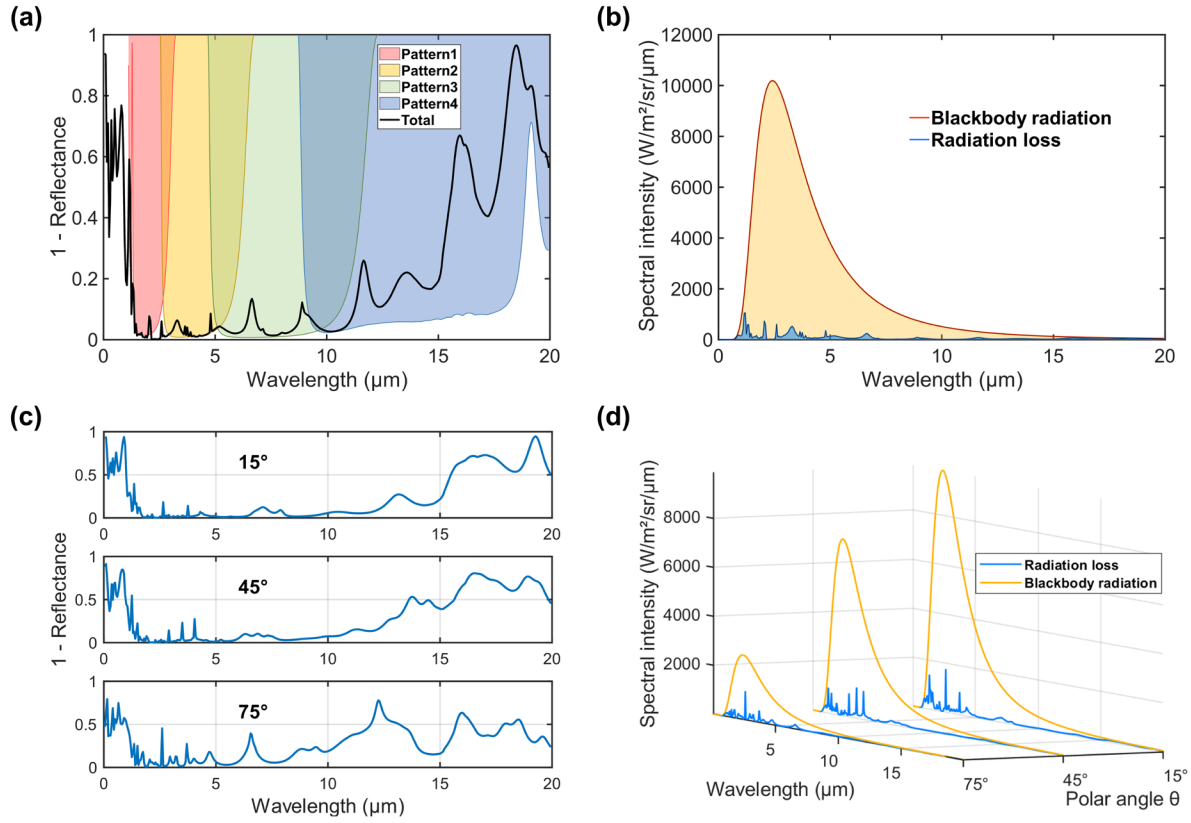

Fig. 3. Performance evaluation of the ODRs optimized for 1200 K heat sources. (a) Normal-incidence radiation loss spectrum (i.e., 1 – reflectance) of an ODR consisting of 4 patterns, with each reflection band highlighted in different colors. (b) Normal-incidence spectral intensity of a blackbody emitter before and after filtering through the ODR. (c) Angle-dependent radiation loss spectra of the ODR (using the average of TE and TM waves). (d) Angle-dependent spectral intensity of a blackbody emitter before and after filtering through the ODR.

For an omnidirectional reflector, angle-dependent analysis provides key insights into the shielding effect in terms of the directional bandgap and heat leakage rate. **Fig. 3**c shows the angle-dependent radiation loss spectra of the ODR optimized for 1200 K. We used the average of TE and TM waves as the incident radiation since typical thermal radiation is non-polarized, with half energy stored in each polarization. The ODR exhibits a behavior similar to that of a conventional Bragg mirror, maintaining high reflectance at small incident angles while gradually diminishing at larger ones. Given that most heat source surfaces can be approximated

as Lambert surfaces with emission intensity following a cosine dependence, the energy loss through the reflector at oblique angles results from both reduced source emission and decreased reflector effectiveness, as shown in **Fig. 3**d. While radiation loss at larger angles contributes less to the overall leakage, it remains non-negligible based on our previous analysis of the angle dependence of blackbody radiation. In fact, the 4th pattern was specifically designed to minimize radiation loss due to reflector degradation at large incident angles.

To substantiate the effectiveness of the differentiated waveband design, we analyzed the roles of the 1st and 4th patterns in our reflector. **Fig. 4**a compares the absorptance spectra with and without the 1st pattern, demonstrating that its presence significantly reduces material absorption up to 2 μm. Since absorption is the primary cause of radiation loss at short wavelengths, the differentiated design of the 1st pattern substantially enhances overall shielding performance. The compensation effect of the 4th pattern is illustrated in **Fig. 4**b. As the incident angle increases, the near-perfect reflection range of the reflector (without the 4th pattern) narrows down and shifts toward shorter wavelengths, consistent with omnidirectional bandgap theory, as highlighted by the yellow-filled blocks. This effect is mitigated by adding a 4th pattern. At small incident angles (<45°), the 4th pattern primarily shields long-wavelength radiation (10–16 μm), functioning as a conventional reflector. As the incident angle increases, it begins to assist the 2nd and 3rd pattern in shielding mid-wavelength radiation (4–12 μm), while its effectiveness at long wavelengths diminishes. Due to the high energy concentration in the mid-wavelength region even at large polar angles, this spectral shift plays a crucial role in enhancing overall reflectance. This phenomenon is further observed in **Fig. 4**c and d, where the boundary of the 4th pattern (~16 μm at 0°) noticeably moves toward shorter wavelengths (~12 μm at 70°) with increasing incident angles. These results indicate that the 4th pattern not only shields long-wavelength radiation at small angles but also compensates for radiation loss in the mid-wavelength range caused by large angles of incidence.

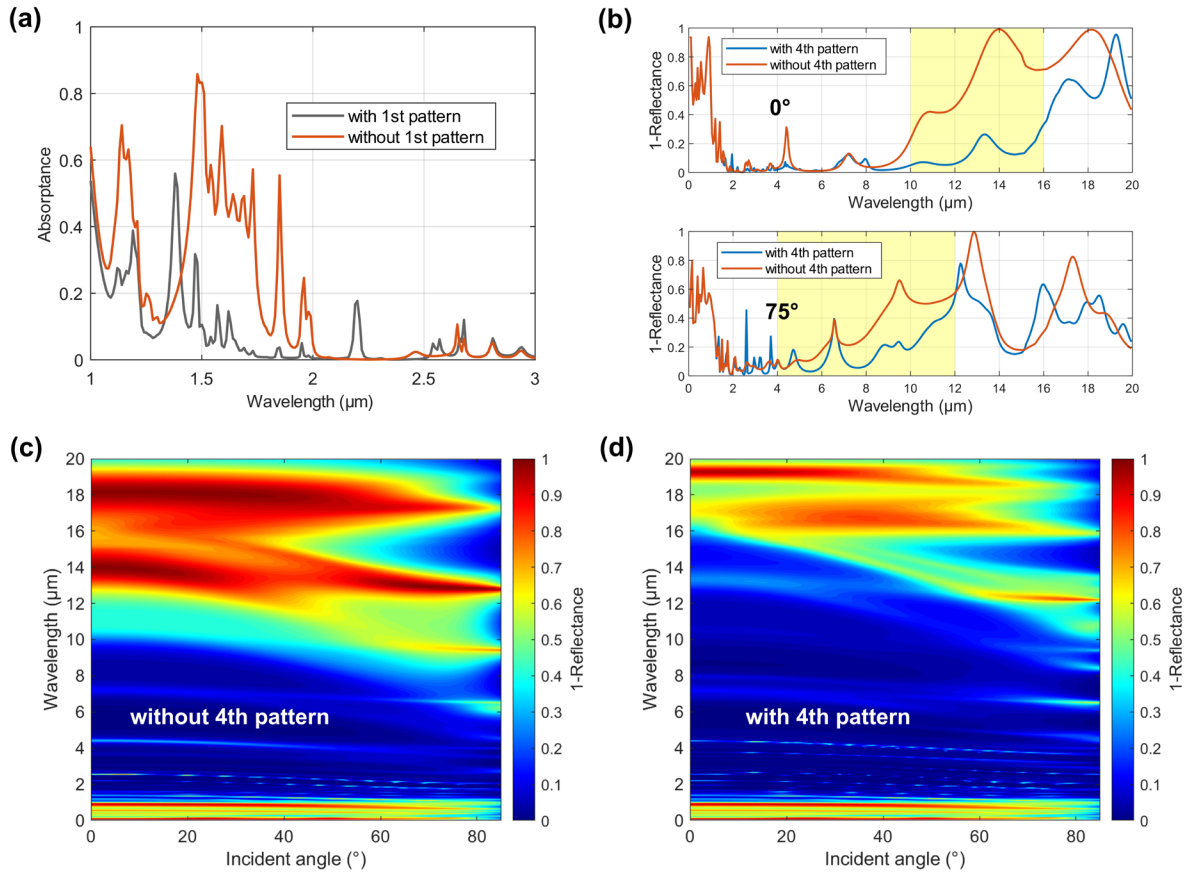

Fig. 4. Evaluation of the differentiated waveband design (optimized for 1200 K). (a) Absorptance spectra of the ODR with/without the 1st pattern at short wavelengths. (b) Radiation loss spectra with/without the 4th pattern at different incident angles. The yellow-filled block highlights the spectral region where the 4th pattern primarily operates. (c) 2D spectrum of the ODR without the 4th pattern as a function of wavelength and incident angle, where color represents radiation loss (i.e., 1 – reflectance). (d) 2D spectrum of the ODR with the 4th pattern.

For an ODR designed for 1200 K, the ideal effective thermal conductivity is calculated to be only 0.000108 W/m·K, significantly lower than that of conventional radiation barriers. We calculated the effective thermal conductivity using Fourier's Law of Heat Conduction [50] and the Stefan–Boltzmann law $k_{eff} = \frac{q''_{conduct}L}{\Delta T} = \eta_{rad}\frac{q''_{incident}L}{\Delta T} = \eta_{rad}\frac{\sigma T^4 L}{\Delta T}$, where $q''_{conduct}$ represents the heat flux conducted through the barrier, $q''_{incident}$ is the incident heat flux from the heat source, σ is the Stefan–Boltzmann constant, T is the heat source temperature, ΔT is the temperature difference, L and η_{rad} represent the thickness and radiation loss of ODR separately. Table 2 provides a comparative analysis of the effective thermal conductivity, heat

retaining rate, and thickness of our ODR relative to other technologies, further highlighting the great potential of this design.

Table 2. Comparison of some thermal radiation barriers with the ODR in this study.

	Refs.	Material composition	Thickness (μm)	Heat source temperature (K)	Heat retaining rate	Thermal conductivity (W/m·K)
Reflective TBCs	14	YSZ-Al_2O_3 stack	132.8	1589	73%	1.2
	16	ZrO_2 3D PhG	100	1173	70%-90%*	0.14
MLIs	23	Steel Foil + Al silicate fiber-aerogel	15,000	1273	-	0.033*
	24	TiN-coated silicon wafer + Silica fiber	3,680	1400	91.57%	0.053*
ODRs	This study	Ge + MgF_2 1D PhC	13	1200	93.5%	0.0001

*Experimental results

In practical applications, the feasibility of an ODR is influenced by several factors, including fabrication costs, process uncertainties, material optical constants, variations in heat source temperature, and material thermal stability. We investigated the potential impact of these factors on the reflector's performance. The current ODR consists of 4 patterns, with each pattern consisting of 2 periods of materials with high and low refractive indices. The four-pattern structure ensures that the cascaded reflection bandwidth adequately covers the blackbody radiation spectrum at around 1200 K. Increasing the number of periods within each pattern can enhance performance but also raises fabrication costs and the risk of structural failure. To assess this trade-off, we conducted simulations based on the ODR optimized for 1200 K, maintaining the number of patterns while varying the period number from 1 to 4. The total number of layers is then 8, 16, 24, and 32. **Fig. 5**a shows the performance of these reflectors with different layer counts. A significant improvement is observed when increasing from 1 to 2 periods, reducing radiation loss from 12.22% to 6.51%. However, the improvement becomes less pronounced beyond 2 periods, with only a marginal 1.02% reduction from 2 to 3 periods and a minimal 0.05% reduction from 3 to 4 periods. These results indicate that a two-period ODR almost approaches the performance limit without the need for additional periods.

Process uncertainty refers to the thickness variation induced by fabrication. In microfabrication, the layer thickness can deviate from the designed value and thus impact performance. To quantify this effect, we performed Monte Carlo simulations by introducing

relative thickness uncertainties based on a fixed Gaussian standard deviation. These uncertainties were applied to the optimized 16-layer structure (1200 K), and simulations were run 100,000 times for each standard deviation. The resulting radiation loss distributions are presented in **Fig. 5**b. The results confirm that any deviation in layer thickness leads to an increase in radiation loss beyond the optimal value (6.51%). When a process has a tighter tolerance in thickness, the thermal leakage is closer to the optimal value with a narrower distribution. A relatively small uncertainty (5%) results in leakage values centered around 6.84%, while larger uncertainties lead to increased thermal leakage. Nevertheless, even with a process uncertainty as large as 13%, the mean thermal leakage remains below 8%, demonstrating that the shielding performance of our ODR is still superior to that of most thermal radiation barriers with similar dimensions.

The variation in material optical constants was also analyzed, but the impact on overall performance was found to be secondary. **Fig. 5**c and d present the refractive indices of Ge and MgF_2 used in optimization (labeled in red) alongside values obtained from other sources [46,47,51–54]. Due to the limited experimental data for MgF_2, DFT computations were performed and incorporated into the analysis. These optical constants from various sources were fed into the optimized structure, with the resulting radiation losses shown as green markers in **Fig. 5**a. A temperature rise from 293 K to 500 K leads to only a 0.33% reduction in performance, while the maximum refractive index variations (labeled in purple in **Fig. 5**c and d) cause a mere 1.16% decrease.

When the ODR operates under off-design conditions, subject to varying source temperatures as seen in many TPV systems, we simulated its performance over a range from 1000 K to 1500 K, using the structure optimized for a 1200 K heat source. The results, shown in **Fig. S4**, indicate that while radiation loss increases slightly as the heat source temperature deviates from 1200 K, it remains below 7.5% across the 500 K variation range, demonstrating the ODR's robust immunity to source temperature fluctuations. Additionally, the high-temperature stability of the ODR has been preliminarily confirmed. The optical constants of both Ge and MgF_2 are consistent across various literature sources (as shown in **Fig. 5**c and d) and remain stable at elevated temperatures [54,55]. Experimentally, we validated the stability of Ge and

MgF_2 films by comparing their optical performance before and after annealing at 700°C for 2 hours, as shown in **Fig. S5** and **Fig. S6**.

In future work, we will focus on overcoming material fabrication challenges and integrating ODRs into TPV systems. A key challenge for layered materials is preserving structural integrity at high temperatures, which can be potentially addressed through tri-phase fabrication or stress-relief coatings [56]. At a system level, integrating the material into a TPV system will require addressing challenges related to structural support, chemical compatibility, and maximum survival temperatures.

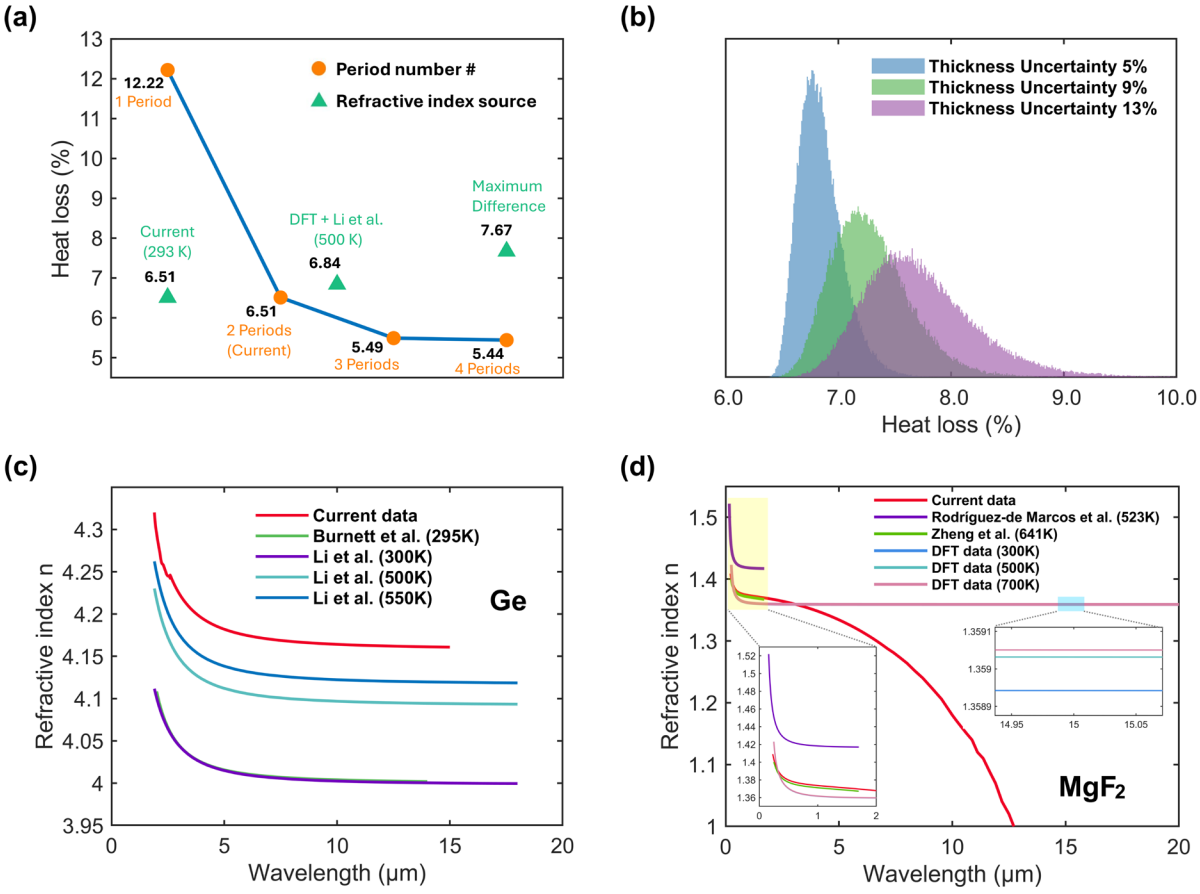

Fig. 5. Performance of ODRs subject to fabrication and material properties uncertainty. (a) Relation between the radiation loss and the number of periods (marked in orange). Radiation losses of the optimal structure calculated using refractive indices from various sources (marked in green). (b) Monte Carlo simulation demonstrating the performance influenced by layer thickness uncertainty in fabrication. (c) and (d) Temperature-dependent refractive indices of Ge and MgF_2 from DFT simulations and other sources [46,47,51–54].

CONCLUSION

In this study, we investigated the potential application of a 1D PhC with the omnidirectional bandgap as a radiative thermal insulator. We designed the insulator based on Ge and MgF_2 for their desirable optical contrasts and fabrication compatibility. A cascaded and differentiated waveband design was adopted to maximize overall reflectance across a broadband spectrum. For a heat source at 1200 K, the optimized photonic design with 16 layers (4 patterns with 2 periods each) can retard roughly 93% of thermal radiation, which is potentially more effective than a refractory metallic shield. The total thickness of such a structure is around 13 μm, significantly more compact than a MLI with similar performance. For heat sources from 800 K to 1400 K, the thermal leakage of the optimized structures is 6.51%–8.44%, while the maximum total thickness does not exceed 21 μm. The differentiated design method was substantiated and can be extended to other broadband photonic designs with similar purposes. An optimal practical solution was proposed with consideration of fabrication costs, thickness uncertainties and variations in material properties. With the continuous shrinking down of thermal-based power generators to portable sizes, the microscale insulator offers a new approach to insulating radiative heat transfer across a small distance with a large thermal gradient, enabling the development of more compact and efficient systems.

ASSOCIATED CONTENT

Supplementary materials

Supplementary data to this article can be found online

AUTHOR INFORMATION

Corresponding Author

*Xiawa Wang: xiawa.wang@dukekunshan.edu.cn

Author Contributions

#Shihe Pan and Yixin Sun contributed equally to this work.

CRediT authorship contribution statement

Shihe Pan: Writing - original draft, Software. Yixin Sun: Writing – original draft, Software. Xiaoquan Liu: Investigation. Xiaoqi Zhou: Investigation. Shipei Zhang: Data curation. Shengyu Sun: Data curation. Xiawa Wang: Writing – review & editing, Conceptualization

Notes

The authors declare no competing financial interests.

ACKNOWLEDGMENTS

This work is supported by NSFC Young Scientist Program 12105124, Gusu Innovation Program ZXL2021252, Jiangsu Shuangchuang Prestigious Ph.D Program, Kunshan Shuangchuang Talent Program kssc202202061, Kunshan Municipal Government Research Fund.

REFERENCES

[1] A. Atkinson, S. Barnett, R.J. Gorte, J.T.S. Irvine, A.J. Mcevoy, M. Mogensen, S.C. Singhal, J. Vohs, Advanced anodes for high-temperature fuel cells, Nat. Mater. 3 (2004) 17–27. https://doi.org/10.1038/nmat1040.

[2] J. Seo, H.-S. Lim, J. Park, M.R. Park, B.S. Choi, Development and experimental investigation of a 500-W class ultra-micro gas turbine power generator, Energy 124 (2017) 9–18. https://doi.org/10.1016/j.energy.2017.02.012.

[3] S. Qiu, Y. Gao, G. Rinker, K. Yanaga, Development of an advanced free-piston Stirling engine for micro combined heating and power application, Appl. Energy 235 (2019) 987–1000. https://doi.org/10.1016/j.apenergy.2018.11.036.

[4] L. Tailin, Comprehensive modeling and characterization of the General-Purpose Heat Source Radioisotope Thermoelectric Generator for solar system missions, Appl. Therm. Eng. (2024).

[5] A. Datas, A. Martí, Thermophotovoltaic energy in space applications: Review and future potential, Sol. Energy Mater. Sol. Cells 161 (2017) 285–296. https://doi.org/10.1016/j.solmat.2016.12.007.
[6] C.J. Crowley, Thermophotovoltaic Converter Performance for Radioisotope Power Systems, in: AIP Conf. Proc., AIP, Albuquerque, New Mexico (USA), 2005: pp. 601–614. https://doi.org/10.1063/1.1867178.
[7] Z. Wang, D. Kortge, Z. He, J. Song, J. Zhu, C. Lee, H. Wang, P. Bermel, Selective emitter materials and designs for high-temperature thermophotovoltaic applications, Sol. Energy Mater. Sol. Cells 238 (2022) 111554. https://doi.org/10.1016/j.solmat.2021.111554.
[8] X. Wang, W. Chan, P. Fisher, R. Liang, J. Xu, Thermal Insulation Design of Portable Radioisotope Electrical Generators, in: 2019 19th Int. Conf. Micro Nanotechnol. Power Gener. Energy Convers. Appl. PowerMEMS, 2019: pp. 1–5. https://doi.org/10.1109/PowerMEMS49317.2019.61547404455.
[9] X. Wang, W. Chan, V. Stelmakh, P. Fisher, Radioisotope Thermophotovoltaic Generator Design and Performance Estimates for Terrestrial Applications, in: Vol. 3 Nucl. Fuel Mater. React. Phys. Transp. Theory Innov. Nucl. Power Plant Des. New Technol. Appl., American Society of Mechanical Engineers, Shanghai, China, 2017: p. V003T13A008. https://doi.org/10.1115/ICONE25-66607.
[10] R.C. Langley, Gold coatings for temperature control in space exploration, Gold Bull. 4 (1971) 62–66. https://doi.org/10.1007/BF03215144.
[11] X. Wang, R. Liang, P. Fisher, W. Chan, J. Xu, Critical design features of thermal-based radioisotope generators: A review of the power solution for polar regions and space, Renew. Sustain. Energy Rev. 119 (2020) 109572. https://doi.org/10.1016/j.rser.2019.109572.
[12] M. Fabian, E. Lewis, T. Newe, S. Lochmann, Optical fibre cavity for ring-down experiments with low coupling losses, Meas. Sci. Technol. 21 (2010) 094034. https://doi.org/10.1088/0957-0233/21/9/094034.
[13] J. Mulla, F. Kaka, R. Satapathy, The emergence of reflective thermal barrier coatings, Crit. Rev. Solid State Mater. Sci. 49 (2024) 582–606. https://doi.org/10.1080/10408436.2023.2245599.
[14] M.J. Kelly, D.E. Wolfe, J. Singh, J. Eldridge, D. Zhu, R. Miller, Thermal Barrier Coatings Design with Increased Reflectivity and Lower Thermal Conductivity for High-Temperature Turbine Applications, Int. J. Appl. Ceram. Technol. 3 (2006) 81–93. https://doi.org/10.1111/j.1744-7402.2006.02073.x.
[15] H.S. Lee, R. Kubrin, R. Zierold, A.Yu. Petrov, K. Nielsch, G.A. Schneider, M. Eich, Thermal radiation transmission and reflection properties of ceramic 3D photonic crystals, J. Opt. Soc. Am. B 29 (2012) 450. https://doi.org/10.1364/JOSAB.29.000450.
[16] P.N. Dyachenko, J.J. do Rosário, E.W. Leib, A.Yu. Petrov, R. Kubrin, G.A. Schneider, H. Weller, T. Vossmeyer, M. Eich, Ceramic Photonic Glass for Broadband Omnidirectional Reflection, ACS Photonics 1 (2014) 1127–1133. https://doi.org/10.1021/ph500224r.
[17] J.J. do Rosário, Y. Häntsch, R.M. Pasquarelli, P.N. Dyachenko, E. Vriend, A.Y. Petrov, K.P. Furlan, M. Eich, G.A. Schneider, Advancing the fabrication of YSZ-inverse photonic glasses for broadband omnidirectional reflector films, J. Eur. Ceram. Soc. 39 (2019) 3353–3363. https://doi.org/10.1016/j.jeurceramsoc.2019.04.028.
[18] A. Gomez-Gomez, D. Ribas Gomes, B.F. Winhard, L.G. Maragno, T. Krekeler, M. Ritter, K.P. Furlan, Mullite photonic glasses with exceptional thermal stability for novel reflective thermal barrier coatings, J. Mater. Sci. 58 (2023) 12993–13008. https://doi.org/10.1007/s10853-023-08844-2.

[19] C.-S. Kang, Multilayer Insulation for Spacecraft Applications, in: F.-B. Hsiao (Ed.), COSPAR Colloq. Ser., Pergamon, 1999: pp. 175–179. https://doi.org/10.1016/S0964-2749(99)80023-7.
[20] P.M. Sutheesh, A. Chollackal, Thermal performance of multilayer insulation: A review, IOP Conf. Ser. Mater. Sci. Eng. 396 (2018) 012061. https://doi.org/10.1088/1757-899X/396/1/012061.
[21] K. Daryabeigi, S.D. Miller, G.R. Cunnington, Heat Transfer in High Temperature Multilayer Insulation, in: Noordwijk, 2007. https://ntrs.nasa.gov/citations/20080013560 (accessed February 20, 2025).
[22] B. Ai, S. Zhang, X. Sun, H. Sun, Y. Chen, K. Fang, D. Yan, Optimization and Application Technology of Reflective Foils Using in Zirconia Fiber Insulation Materials, IOP Conf. Ser. Mater. Sci. Eng. 678 (2019) 012099. https://doi.org/10.1088/1757-899X/678/1/012099.
[23] M. Wang, J. Feng, Y. Jiang, Z. Zhang, J. Feng, Preparation and properties of the multi-layer aerogel thermal insulation composites, Heat Mass Transf. 54 (2018) 2793–2798. https://doi.org/10.1007/s00231-018-2320-8.
[24] X. Zhou, D. Li, J. Zhang, X. Wang, P. Fisher, Y. Sun, S. Pan, S. Zhang, L. Qiu, X. Wang, Modeling and implementation of multilayer insulation for small-scale ultrahigh temperature systems, Appl. Therm. Eng. 245 (2024) 122838. https://doi.org/10.1016/j.applthermaleng.2024.122838.
[25] J.N. Winn, Y. Fink, S. Fan, J.D. Joannopoulos, Omnidirectional reflection from a one-dimensional photonic crystal, Opt. Lett. 23 (1998) 1573. https://doi.org/10.1364/OL.23.001573.
[26] Y. Fink, J.N. Winn, S. Fan, C. Chen, J. Michel, J.D. Joannopoulos, E.L. Thomas, A Dielectric Omnidirectional Reflector, Science 282 (1998) 1679–1682. https://doi.org/10.1126/science.282.5394.1679.
[27] W. Li, L. Morales-Inostroza, W. Xu, P. Zhang, J. Renger, S. Götzinger, X.-W. Chen, Truncated Metallo-Dielectric Omnidirectional Reflector: Collecting Single Photons in the Fundamental Gaussian Mode with 95% Efficiency, ACS Photonics 7 (2020) 2474–2481. https://doi.org/10.1021/acsphotonics.0c00730.
[28] G. Xu, Q. Kang, X. Zhang, W. Wang, K. Guo, Z. Guo, Inverse-design laser-infrared compatible stealth with thermal management enabled by wavelength-selective thermal emitter, Appl. Therm. Eng. 255 (2024) 124063. https://doi.org/10.1016/j.applthermaleng.2024.124063.
[29] W. Lin, G.P. Wang *, S. Zhang, Design and fabrication of omnidirectional reflectors in the visible range, J. Mod. Opt. 52 (2005) 1155–1160. https://doi.org/10.1080/09500340512331327606.
[30] D.N. Chigrin, A.V. Lavrinenko, D.A. Yarotsky, S.V. Gaponenko, All-dielectric one-dimensional periodic structures for total omnidirectional reflection and partial spontaneous emission control, J. Light. Technol. 17 (1999) 2018–2024. https://doi.org/10.1109/50.802989.
[31] M. Deopura, C.K. Ullal, B. Temelkuran, Y. Fink, Dielectric omnidirectional visible reflector, Opt. Lett. 26 (2001) 1197. https://doi.org/10.1364/OL.26.001197.
[32] Y. Park, Y.-G. Roh, C.-O. Cho, H. Jeon, M.G. Sung, J.C. Woo, GaAs-based near-infrared omnidirectional reflector, Appl. Phys. Lett. 82 (2003) 2770–2772. https://doi.org/10.1063/1.1569045.
[33] S.K. Srivastava, S.P. Ojha, Broadband optical reflector based on Si/SiO_2 one-dimensional graded photonic crystal structure, J. Mod. Opt. 56 (2009) 33–40. https://doi.org/10.1080/09500340802428330.
[34] D. Jain, Kh.S. Singh, V. Kumar, S. Sharma, M.P.S. Rao, Design of an omni-directional reflector using 1D ge-based photonic crystal, in: Bikaner, Rajasthan, India, 2013: pp. 707–708. https://doi.org/10.1063/1.4810423.

[35] Z. Omair, S. Hooten, E. Yablonovitch, Broadband mirrors with >99% reflectivity for ultra-efficient thermophotovoltaic power conversion, in: A.K. Dutta, P. Balaya, S. Xu (Eds.), Energy Harvest. Storage Mater. Devices Appl. XI, SPIE, Online Only, United States, 2021: p. 5. https://doi.org/10.1117/12.2588738.

[36] O. Del Barco, E.C. Jarque, V. Gasparian, J.M. Bueno, Omnidirectional high-reflectivity mirror in the 4–20 μ m spectral range, J. Opt. 19 (2017) 065102. https://doi.org/10.1088/2040-8986/aa6c76.

[37] X. Wang, X. Hu, Y. Li, W. Jia, C. Xu, X. Liu, J. Zi, Enlargement of omnidirectional total reflection frequency range in one-dimensional photonic crystals by using photonic heterostructures, Appl. Phys. Lett. 80 (2002) 4291–4293. https://doi.org/10.1063/1.1484547.

[38] Z.M. Jiang, B. Shi, D.T. Zhao, J. Liu, X. Wang, Silicon-based photonic crystal heterostructure, Appl. Phys. Lett. 79 (2001) 3395–3397. https://doi.org/10.1063/1.1421093.

[39] D.T. Zhao, H. Zhou, Z.M. Jiang, Y.L. Fan, X. Wang, Fabrication and performance of a medium-dependent SiO_2/Si photonic heterostructure device, Opt. Lett. 28 (2003) 843. https://doi.org/10.1364/OL.28.000843.

[40] P. Han, H. Wang, Criterion of omnidirectional reflection in a one-dimensional photonic heterostructure, J. Opt. Soc. Am. B 22 (2005) 1571. https://doi.org/10.1364/JOSAB.22.001571.

[41] J. Zhang, T.M. Benson, Design of omnidirectional reflectors based on a cascaded one-dimensional photonic crystal structure, J. Mod. Opt. 60 (2013) 1804–1812. https://doi.org/10.1080/09500340.2013.863400.

[42] J.D. Joannopoulos, ed., Photonic crystals: molding the flow of light, 2nd ed, Princeton University Press, Princeton, 2008.

[43] C. Ou, J. Wang, C. Sun, Z. Hao, Y. Han, B. Xiong, L. Wang, H. Li, J. Yu, Y. Luo, A high-Q mid-infrared Tamm plasmon absorber using MgF_2 and Ge aperiodic tandem films designed by the genetic algorithm, AIP Adv. 12 (2022) 035052. https://doi.org/10.1063/5.0086863.

[44] M.F. Modest, Radiative heat transfer, Third edition, Elsevier Science, San Diego, 2013.

[45] V. Liu, S. Fan, S4 : A free electromagnetic solver for layered periodic structures, Comput. Phys. Commun. 183 (2012) 2233–2244. https://doi.org/10.1016/j.cpc.2012.04.026.

[46] T. Amotchkina, M. Trubetskov, D. Hahner, V. Pervak, Characterization of e-beam evaporated Ge, YbF_3, ZnS, and LaF_3 thin films for laser-oriented coatings, Appl. Opt. 59 (2020) A40. https://doi.org/10.1364/AO.59.000A40.

[47] E.D. Palik, G. Ghosh, eds., Handbook of optical constants of solids, Academic Press, San Diego, 1998.

[48] P. Giannozzi, S. Baroni, N. Bonini, M. Calandra, R. Car, C. Cavazzoni, D. Ceresoli, G.L. Chiarotti, M. Cococcioni, I. Dabo, A.D. Corso, S. de Gironcoli, S. Fabris, G. Fratesi, R. Gebauer, U. Gerstmann, C. Gougoussis, A. Kokalj, M. Lazzeri, L. Martin-Samos, N. Marzari, F. Mauri, R. Mazzarello, S. Paolini, A. Pasquarello, L. Paulatto, C. Sbraccia, S. Scandolo, G. Sclauzero, A.P. Seitsonen, A. Smogunov, P. Umari, R.M. Wentzcovitch, QUANTUM ESPRESSO: a modular and open-source software project for quantum simulations of materials, J. Phys. Condens. Matter 21 (2009) 395502. https://doi.org/10.1088/0953-8984/21/39/395502.

[49] A. Marini, C. Hogan, M. Grüning, D. Varsano, yambo: An ab initio tool for excited state calculations, Comput. Phys. Commun. 180 (2009) 1392–1403. https://doi.org/10.1016/j.cpc.2009.02.003.

[50] F.P. Incropera, F.P. Incropera, eds., Fundamentals of heat and mass transfer, 6th ed, John Wiley,

Hoboken, NJ, 2007.
[51] H.H. Li, Refractive index of silicon and germanium and its wavelength and temperature derivatives, J. Phys. Chem. Ref. Data 9 (1980) 561–658. https://doi.org/10.1063/1.555624.
[52] J.H. Burnett, S.G. Kaplan, E. Stover, A. Phenis, Refractive index measurements of Ge, in: P.D. LeVan, A.K. Sood, P. Wijewarnasuriya, A.I. D'Souza (Eds.), San Diego, California, United States, 2016: p. 99740X. https://doi.org/10.1117/12.2237978.
[53] L.V. Rodríguez-de Marcos, J.I. Larruquert, J.A. Méndez, J.A. Aznárez, Self-consistent optical constants of MgF2, LaF3, and CeF3 films, Opt. Mater. Express 7 (2017) 989. https://doi.org/10.1364/OME.7.000989.
[54] Q. Zheng, X. Wang, D. Thompson, Temperature-dependent optical properties of monocrystalline CaF2, BaF2, and MgF2, Opt. Mater. Express 13 (2023) 2380. https://doi.org/10.1364/OME.496246.
[55] H.K. Chen, Y.Y. Jie, L. Chang, Oxidation characteristics of MgF_2 in air at high temperature, IOP Conf. Ser. Mater. Sci. Eng. 170 (2017) 012035. https://doi.org/10.1088/1757-899X/170/1/012035.